Multi-Objective Topology Optimization of Wing Skeletons for Aeroelastic Membrane Structures

Bret Stanford[1] and Peter Ifju[2]
University of Florida, Gainesville, FL, 32607
bstan@ufl.edu

ABSTRACT

This work considers the multi-objective aeroelastic optimization of a membrane micro air vehicle wing through topology optimization. The low aspect ratio wing is discretized into panels: a two material formulation on the wetted surface is used, where each panel can be membrane (wing skin) or carbon fiber (laminate reinforcement). An analytical sensitivity analysis of the aeroelastic system is used for the gradient-based optimization of aerodynamic objective functions. An explicit penalty is added, as needed, to force the structure to a 0–1 distribution. Pareto trade-off curves are constructed by considering convex combinations of two disparate lift, drag, or pitching moment-based objective functions. The general relationship between spatial stiffness distribution (wing topology) and aerodynamic performance is discussed, followed by the Pareto optimality of the computed designs over a series of baseline wing structures. The work concludes with an experimental validation of the superiority of select optimal designs.

NOMENCLATURE

$\mathbf{a}$	adjoint vector
$\mathbf{A}$	aeroelastic Jacobian
α	angle of attack
b	wingspan
β	small number to prevent singularity
c	root chord
$\mathbf{C}$	vortex lattice influence matrix
C_D	drag coefficient
C_L	lift coefficient
$C_{L\alpha}$	lift slope
$C_{m\alpha}$	pitching moment slope
D	carbon fiber flexural rigidity
f_1, f_2	conflicting objective functions
g	convex combination of objective functions
$\mathbf{G}$	aeroelastic system of equations
$\mathbf{\Gamma}$	horseshoe vortex circulations
$\mathbf{K}$	reduced global stiffness matrix
$\mathbf{K}_e$	element stiffness matrix
$\mathbf{K}_p$, $\mathbf{K}_m$	carbon fiber and membrane stiffness matrices
$\mathbf{L}$	vortex lattice source vector
L/D	efficiency
$\mathbf{n}$	wing outward normal
p	nonlinear power law
$\mathbf{P}$, $\mathbf{Q}$	interpolation matrices
$\mathbf{r}$	aeroelastic response
R	penalty parameter

[1]Research Assistant, Department of Mechanical and Aerospace Engineering; currently National Research Council Postdoctoral Fellow, U.S. Air Force Research Laboratory, Wright-Patterson Air Force Base.

[2]Professor, Department of Mechanical and Aerospace Engineering.

S	sensitivity of objective function to vortex circulations
T	in-plane membrane pre-stress resultant
u	solution to finite element analysis
u_o, v_o, w_o	induced velocities
U_∞	free-stream velocity
w	out-of-plane displacement
x, y	chordwise and spanwise position
X	element densities
$\mathbf{z_o}$, **z**	rigid and flexible wing shapes
δ	weighting parameter

1. INTRODUCTION

The structural design of thin flexible wings for micro and small unmanned air vehicles, as well as larger wings for hang gliders and sail structures, can take a great deal of inspiration from biological flyers. These animals, covering a large range of wing spans, flight speeds, and wing beat frequencies, almost universally utilize a bi-material wing structure, consisting of a thin, flexible membrane-type sheet, affixed to a stiffer interconnected network, hereafter labeled as a wing "skeleton". The venation patterns of insect wings show substantial variations from one species to the next, providing a significant degree of passive twist and/or cambering during the wing stroke[1]. As one moves to larger creatures, the term "skeleton" becomes more appropriate: finger bones typically provide the underlying network to support the flexible wing. Avian flight obviously utilizes an array of feathers to form a lifting surface[2], while bats are equipped with a monolithic membrane skin stretched over the bones[3]. A similar membrane/bone arrangement is found in the remains of pterosaur wings[4]. Unlike insects, these three animals are/were able to actively shape their wings to beneficially affect both forward and flapping flight: wing warping, twisting, and membrane tension control are all prevalent.

The artificial analogy to the wings described above can take many forms; a thoroughly-studied structure for fixed-wing micro air vehicles (MAVs) utilizes an elastic latex membrane skin sealed to a carbon fiber wing skeleton[5]. Such a vehicle is beset by a number of unfavorable aerodynamic issues, due to the low Reynolds number flow (10^4–10^5) over the low aspect ratio (~1) wing. The passive shape adaptation of the membrane wing can potentially alleviate these issues, but exactly how the membrane skin interacts with the surrounding flow depends upon the layout of the wing skeleton. From a numerical modeling standpoint, the conceptual design of a wing skeleton essentially represents an aeroelastic topology optimization problem. The wing surface is discretized into a series of panels, and each represents a binary variable: the panel is either membrane skin, or carbon fiber laminate. Objective functions can include aerodynamic efficiency, agility, stability, or a compromise between these disparate metrics. This work is particularly concerned with the latter option, utilizing a multi-objective optimization approach to develop a series of trade-off curves.

Extensive reviews of topology optimization can be found in the work of Eschenauer and Olhoff[6], Bendsøe et al.[7], and Patel et al.[8] As mentioned above, the design domain is discretized, and the relative density of each element can be 0 (void) or 1 (solid). Due to the difficulties in optimizing such a large binary problem, the design variables are typically allowed to vary continuously between 0 and 1, with intermediate values penalized in some fasion[6] during the optimization process. Multi-objective topology optimization strategies are given by Chen and Wu[9], Nishiwaki et al.[10], and Min et al.[11] Despite the use of topology optimization for a wide range of technical disciplines in recent years[7], its use in aeronautical applications is relatively rare, while aeroelastic applications are rarer still.

The literature pertaining to wing design via topology optimization can be broken into two rough categories. The first uses an aerodynamic solver to compute the pressure distribution over the wing (during steady flight, pull-up maneuvers, etc). This load distribution is then applied to the structure for optimization: global metrics such as compliance, weight/volume fraction, and vibration frequency or local metrics such as displacement and stress objective functions and constraints can all be considered. The re-distribution of the aerodynamic loading due to elastic wing deformation is ignored. The second category explicitly uses the aerodynamic performance of a flexible wing for objective functions or constraints, and necessarily includes aeroelastic coupling.

Literature indicative of the first category can be found in the work of Balabanov and Haftka[12], who optimize the internal structure of a transport wing for compliance minimization. Eschenauer and

Olhoff[6] optimize the topology of an internal wing rib under both pull-up load maneuvers and internal tank pressures, using a bubble method. Krog et al.[13] also optimize the topology of wing box ribs, and discuss methods for interpretation of the results to form an engineering design, followed by sizing and shape optimization. Luo et al.[14] compute the optimal topology of an aerodynamic missile body, considering both static loads and natural frequencies.

Aeroelastic topology optimization (second category discussed above) is utilized by Maute and Allen[15], who consider the topological layout of stiffeners within a swept wing, using a three-dimensional Euler solver coupled to a linear finite element model. Results from an adjoint sensitivity analysis of the coupled aeroelastic system are used to minimize mass with constraints upon the lift, drag, and wing displacement. This research effort is extended by Maute and Reich[16] for topology optimization of a compliant morphing mechanism within an airfoil, considering both passive and active shape deformations. Very recent work is given by Gomes and Suleman[17], who use a spectral level set method to maximize aileron reversal speed by reinforcing the upper skin of a wing torsion box via topology optimization.

As the current work is concerned with aeroelastic topology optimization, the latter three research efforts are particularly relevant, though active morphing[16] and lateral maneuvers[17] are beyond the scope intended here. This leaves the work of Maute and Allen[15] as a pertinent reference point for the current research; the authors decisively demonstrate the importance of including aeroelastic load redistributions (rather than the pure structural optimization approach of Krog et al.[13], among others listed above), but are prohibited (by the extremely large size of the systems under consideration) from thoroughly studying the effect of the objective function and the constraint boundaries upon the optimal wing topology. Such an issue may be of more importance for MAVs than the larger vehicles studied by Maute and Allen, expected to demonstrate a wide range of flight capabilities either remotely or by autopilot. The original contribution of this work is to use a lower fidelity aeroelastic solver capable of multiple runs in conjunction with a multi-objective optimizer, in order to assess the changes in wing topology as the desired wing response is altered: stability, efficiency, drag reduction, etc. The multi-objective optimizer itself (a weighted-sum approach) is not novel, but the resulting Pareto front of wing structures will provide a useful set of guidelines for the aeroelastic design of micro air vehicle wing structures. Experimental validation can then be used to ensure that the underlying physics computed by the lower fidelity model are providing useful results.

The remainder of this work is organized as follows. A brief description of membrane micro air vehicle aeroelasticity is given, followed by details of the topology optimization within the wing structure, and a graphical description of existing baseline wing structures. This is followed by the computational framework: material interpolation, the static aeroelastic model, sensitivity analysis, and multi-objective optimization procedures. A brief discussion of optimal topologies computed for single-objective optimization is given, to provide an understanding of the relationship between spatial stiffness distribution and aerodynamic performance of membrane MAV wings. Results are then given in terms of Pareto optimality and trade-off curves between disparate objective functions. The work is concluded with an experimental validation of the superiority of select optimal designs over baseline wings.

2. MEMBRANE WING STRUCTURES

A flexible MAV wing topological optimization procedure has some precedence in early micro air vehicle work by Ifju et al.[18], with an array of successfully flight tested designs shown in Figure 1. Each of these designs consists of a laminated leading edge, wing tip, and wing root; a series of thin strips of carbon fiber are imbedded within the concomitant membrane skin. All of the designs are qualitatively ranked based upon observations in the field and pilot-reported handling qualities: a crude trial and error process lead to the batten-reinforced design (BR, first row, third column), where three carbon fiber strips (battens) are imbedded into each membrane semi-wing. The trailing edge of this design is permitted to lift up due to an applied pressure load. The nose-down geometric twist of each wing section will alleviate the flight loads, and possibly decrease C_D and $C_{L\alpha}$ (as compared to a rigid wing)[5]. Extensive flight testing has also been conducted upon a perimeter-reinforced MAV design (PR, fourth row, first column). Now the trailing edge is constrained by a laminate perimeter, and the membrane skin will inflate due to an applied load. This aerodynamic twist of each flexible wing section will augment the flight loads, and possibly increase C_L and decrease $C_{m\alpha}$[5]. The vehicles that actually implement these two designs can be seen in Figure 2.

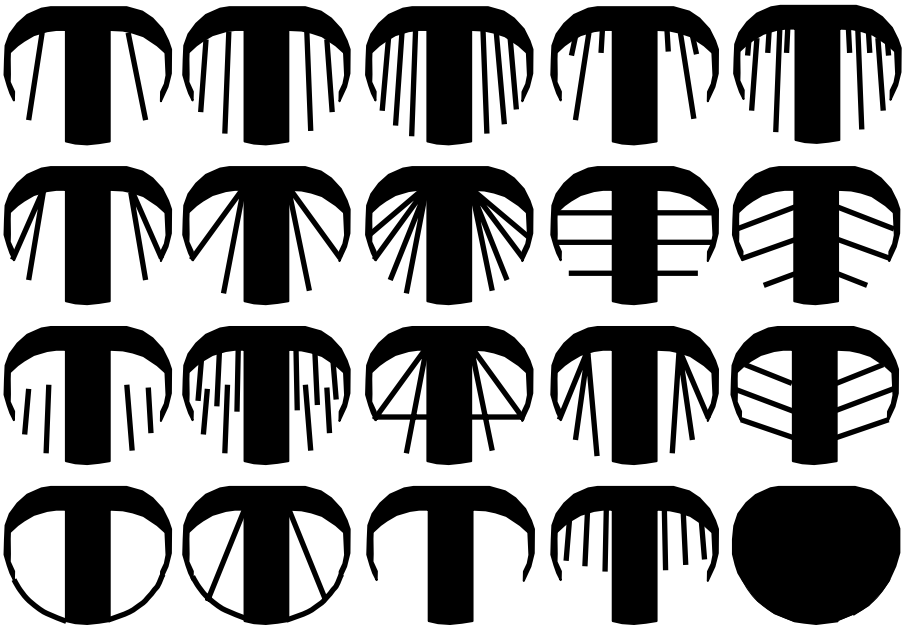

Figure 1. Wing topologies flight tested by Ifju et al.[18]

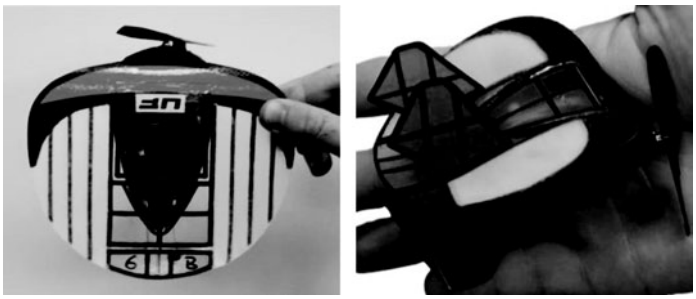

Figure 2. Batten-reinforced (left) and perimeter-reinforced (right) membrane wing designs.

A rigorous aeroelastic topology optimization of the membrane wings may be able to produce structures that out-perform the wings currently used for flight testing (Figure 1), but also (and perhaps more importantly), this work can identify the set of compromise wing topologies that lie along the Pareto optimal front. This requires successive optimizations of a convex combination of the two weighted metrics to fill out the trade-off curve (assuming that this Pareto front is convex). Optimization variables, for this work, will include lift, drag, and pitching moment-based stability and efficiency metrics. The final optimal design can then be selected from the Pareto front based upon metrics not considered in the formal optimization: trim requirements, manufacturability, etc.

A fairly fine structural grid is needed to resolve topologies on the order of those seen in Figure 1, which will, of course, increase the computational cost associated with the optimization. The wing is

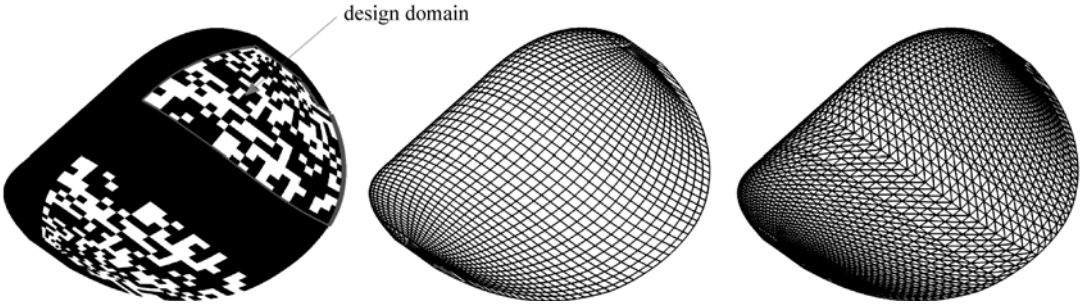

Figure 3. Sample wing topology (left), aerodynamic mesh (center), and structural mesh (right).

discretized into a set of quadrilaterals, which represent the density variables: 0 or 1. These quadrilaterals are used as panels for the aerodynamic solver, and broken into two triangles for the finite element solver, as shown in Figure 3. As in Figure 1, the wing topology at the root, leading edge, and wing tip is fixed as carbon fiber, to maintain some semblance of an aerodynamic shape capable of sustaining lift. The wing topology in the figure is randomly distributed.

3. COMPUTATIONAL FRAMEWORK

3.1. Material Interpolation

As discussed above, topology optimization problems with strictly binary variables can be difficult to solve; a fairly common technique is to allow the relative density of each panel to vary in a continuous manner between 0 and 1. Topology optimization with continuous density variables may require a mechanism to push the final structure to a 0–1 distribution. An implicit penalty upon intermediate densities can be achieved through a nonlinear power law interpolation. This technique is known as the solid isotropic material with penalization method, or SIMP[6]. The power law's effectiveness as an implicit penalty is predicated upon a volume constraint: intermediate densities are unfavorable, as their stiffness is small compared to their volume[19]. For the two-material wing considered above (membrane or carbon fiber), the stiffness matrix $\mathbf{K}_e$ of each finite element in Figure 3. can be computed as:

$$\mathbf{K}_e = \left(\mathbf{K}_p \cdot (1-\beta) - \mathbf{K}_m\right) \cdot X_e^p + \mathbf{K}_m + \beta \cdot \mathbf{K}_p \tag{1}$$

where $\mathbf{K}_p$ and $\mathbf{K}_m$ are the plate and membrane elements, respectively (the latter with zeros placed within rows and columns corresponding to bending degrees of freedom). β is a small number used to prevent singularity in the pure membrane element (due to the bending degrees of freedom), X_e is the density of the element, varying from 0 (membrane) to 1 (carbon fiber), and p is the nonlinear penalization power.

No volume constraint is utilized here, due to an uncertainty upon what this value should be. Furthermore, for aeronautical applications it may be desired to minimize the mass of the wing itself, as discussed by Maute and Allen[15]. Regardless, the nonlinear power law of SIMP is still useful for the current application, as demonstrated by Stanford and Ifju[20]: the stiffness of the membrane skin and the carbon fiber laminate are separated by several orders of magnitude. The nonlinear power law can help smooth the interpolation function; otherwise lift and drag metrics see very large gradients as X_e approaches zero.

As SIMP no longer provides an implicit penalty upon intermediate densities during the optimization process, an explicit penalty is added to the objective function[9] for his work:

$$R \cdot \sum_{i=1}^{N_X} \sin\left(X_i \cdot \pi\right) \tag{2}$$

where R is a penalty parameter appropriately sized so as not to overwhelm the aerodynamic performance of the wing topology. Several potential issues may appear with this formulation: the inclusion of a large penalty early in the optimization process will upset the compromise between improving the aerodynamic performance and removing intermediate densities. In order to prevent such interference, this penalty is only added when and if the aeroelastic optimizer has converged upon a design with intermediate densities. R is sized such that the penalty is 10–15% of the objective function, and is not increased during the optimization process. Such a strategy is not found to significantly alter the optimal topology, as will be discussed below.

3.2. Static Aeroelastic Analysis

Due to the large number of expected function evaluations (~ 200) needed to converge upon an optimal wing topology, and the required aeroelastic sensitivities (computed with an adjoint method), a lower-fidelity aeroelastic model is used for the current application. The membrane elements within the structure are assumed to obey Poisson's differential equation for a taught elastic membrane subjected to a transverse distributed pressure[21]:

$$\nabla^2 w = -p/T \tag{3}$$

where p is the applied pressure, w is the out-of-plane displacement, and T is the in-plane pre-stress resultant. This linear membrane model is known to be accurate, as long as the plane strains that develop

within the elastic sheet due to the pressure loading are much smaller than the original pre-strains. Discretization of the wing into finite elements leaves one degree of freedom per membrane node: the out-of-plane displacement w. The carbon fiber elements of the wing are governed by:

$$\nabla^4 w = p/D \tag{4}$$

where D is the plate's flexural rigidity, and the orthotropy of the laminate is ignored. Each node of a plate element has 3 degrees of freedom: an out-of-plane displacement, and two rotations. The finite element mesh is seen on the right of Figure 3.

A linear vortex lattice method is used to compute the aerodynamic pressure distribution over the flexible wing. The continuous distribution of bound vorticity is approximated by discretizing the wing into a paneled grid, and placing a horseshoe vortex upon each panel. Each horseshoe vortex is comprised of a bound vortex (which coincides with the quarter-chord line of each panel), and two trailing vortices extending downstream. Each vortex filament creates a velocity whose magnitude is assumed to be governed by the Biot-Savart law[22]. Furthermore, a control point is placed at the three-quarter-chord point of each panel. The tangency condition is applied (i.e., the wing becomes a streamline of the flow) by stipulating that the induced flow (from the horseshoe vortices) along the outward normal at each control point exactly cancels with that caused by the free-stream velocity. The following system of equations results:

$$\begin{bmatrix} C_{11} & C_{12} & \cdots & C_{1N} \\ C_{21} & C_{22} & \cdots & C_{2N} \\ \vdots & \vdots & \ddots & \vdots \\ C_{N1} & C_{N2} & \cdots & C_{NN} \end{bmatrix} \cdot \begin{Bmatrix} \Gamma_1 \\ \Gamma_2 \\ \vdots \\ \Gamma_N \end{Bmatrix} = - \begin{Bmatrix} \left\{U_\infty \cos(\alpha), 0, U_\infty \sin(\alpha)\right\} \cdot n_1 \\ \left\{U_\infty \cos(\alpha), 0, U_\infty \sin(\alpha)\right\} \cdot n_2 \\ \vdots \\ \left\{U_\infty \cos(\alpha), 0, U_\infty \sin(\alpha)\right\} \cdot n_N \end{Bmatrix} \tag{5}$$

The source vector in Eq. 5 assumes longitudinal flow (no side-slip): U_∞ is the free-stream velocity, α is the angle of attack of the wing, and n_i is the outward normal of the wing at the i^{th} control point. Γ_i is the unknown circulation strength of each horseshoe vortex, and the influence coefficients are given by:

$$C_{ij} = \left\{u_o \quad v_o \quad w_o\right\}_{ij} \cdot n_i \tag{6}$$

where $u_{o,ij}$, $v_{o,ij}$, and $w_{o,ij}$ are the velocities induced at the i^{th} control point by the j^{th} horseshoe vortex. Further information on the vortex lattice method used here can be found by Katz and Plotkin[22]. Propeller, fuselage, and stabilizers are not included in the analysis, and the resulting aerodynamic mesh is given in the center of Figure 3.

Drag computations present a problem for this inviscid modeling technique, which can only provide induced drag due to lift (the downwash of the finite span deflects the local velocity vector at each wing section downward, tilting the lift vector slightly backward to provide a small drag force): drag due to flow separation and viscous shear is unaccounted for. The latter terms are included by augmenting the drag with a non-zero C_{Do}, estimated from experimental data to be 0.05. The viscous drag terms are not truly constant (flow separation generally increases with angle of attack, for example), and so the vortex lattice method is expected to under-predict the overall drag. Previous work has shown this method to provide an adequate computation of drag (as well as lift and pitching moments) at moderate angles of attack, as compared to wind tunnel data, for micro air vehicle wings[23]. It should also be noted here that higher-fidelity aerodynamic modeling techniques are available: unsteady methods that model the wing-wake interactions, as well as panel methods suitable for simulations of entire vehicles.

Aeroelastic coupling is facilitated by considering the system as defined by a three field response vector **r**:

$$\mathbf{r} = \left\{\mathbf{u}^T \quad \mathbf{z}^T \quad \mathbf{\Gamma}^T\right\}^T \tag{7}$$

where **u** is the solution to the system of finite element equations (composed of both displacements and rotations) at each free node, **z** is the shape of the flexible wing, and Γ is the vector of unknown horseshoe vortex circulations (the solution vector of Eq. 5). The coupled system of equations G(r) is then:

$$\mathbf{G}(\mathbf{r}) = \begin{Bmatrix} \mathbf{K}\cdot\mathbf{u} - \mathbf{Q}\cdot\boldsymbol{\Gamma} \\ \mathbf{z} - \mathbf{z}_o - \mathbf{P}\cdot\mathbf{u} \\ \mathbf{C}\cdot\boldsymbol{\Gamma} - \mathbf{L} \end{Bmatrix} = \mathbf{0} \tag{8}$$

The first row of **G** is the finite element analysis: **K** is the stiffness matrix assembled from the elemental matrices, and appropriately reduced based upon fixed boundary conditions along the wing root. **Q** is an interpolation matrix that converts the circulation of each horseshoe vortex into a pressure, and subsequently into the transverse force at each free node. The second row of **G** is a simple grid regeneration analysis: $\mathbf{z}_o$ is the original (rigid) wing shape, and **P** is a second interpolation matrix that converts the finite element state vector into displacements at each free and fixed node along the wing. The third row of **G** is the vortex lattice method, rewritten from Eq. 5: **C** is the influence matrix depending solely on the wing geometry, and **L** is the source vector depending on the wing's outward normal vectors, the angle of attack, and the free stream velocity. Convergence of this system can typically be obtained within 25 iterations, when the logarithmic error in the wing's lift coefficient is less than –5.

3.3. Adjoint Sensitivity Analysis

As the number of variables in the aeroelastic system (essentially the density of each element) will always outnumber the constraints and objective functions, a sensitivity analysis can be most effectively carried out with an adjoint analysis. The sought-after total derivative of the objective function with respect to each density variable is given through the chain rule:

$$\frac{\mathrm{d}g}{\mathrm{d}\mathbf{X}} = \frac{\partial g}{\partial \mathbf{X}} + \frac{\partial g^{\mathrm{T}}}{\partial \mathbf{r}} \cdot \frac{\mathrm{d}\mathbf{r}}{\mathrm{d}\mathbf{X}} \tag{9}$$

where g is the objective function and **r** is the aeroelastic state vector of Eq. 7. The term $\partial g/\partial \mathbf{X}$ is the explicit portion of the derivative, while the latter term is the implicit portion through dependence on the aeroelastic system[24]. Only aerodynamic objective functions are considered in this work: the explicit portion is then zero, unless the intermediate density penalty (Eq. 2) is included.

The derivative of the objective function with respect to the aeroelastic state vector is:

$$\frac{\partial g}{\partial \mathbf{r}} = \left\{ \mathbf{0} \quad \mathbf{0} \quad \mathbf{S}^{\mathrm{T}} \right\}^{\mathrm{T}} \tag{10}$$

where **S** is the derivative of the aerodynamic objective function with respect to the vector of horseshoe vortex circulations. For metrics such as lift and pitching moment, $g = \mathbf{S}^{\mathrm{T}}\cdot\boldsymbol{\Gamma}$, though more complex expressions exist for drag-based metrics. The derivative of the aeroelastic state vector with respect to the element densities is found by differentiating the coupled system:

$$\frac{\mathrm{d}\mathbf{G}(\mathbf{X}, \mathbf{r})}{\mathrm{d}\mathbf{X}} = 0 \rightarrow \frac{\partial \mathbf{G}}{\partial \mathbf{X}} + \mathbf{A}\cdot\frac{\mathrm{d}\mathbf{r}}{\mathrm{d}\mathbf{X}} = \mathbf{0} \tag{11}$$

Only the finite element analysis of the aeroelastic system contains the element densities, and so the derivative of the aeroelastic system with respect to the density variables is then:

$$\frac{\partial \mathbf{G}}{\partial \mathbf{X}} = \begin{bmatrix} \dfrac{\partial \mathbf{K}}{\partial \mathbf{X}}\cdot\mathbf{u} \\ \mathbf{0} \\ \mathbf{0} \end{bmatrix} \tag{12}$$

A is the Jacobian of the aeroelastic system, defined by:

$$\mathbf{A} = \frac{\partial \mathbf{G}}{\partial \mathbf{r}} = \begin{bmatrix} \mathbf{K} & \mathbf{0} & -\mathbf{Q} \\ -\mathbf{P} & \mathbf{I} & \mathbf{0} \\ \mathbf{0} & \dfrac{\mathrm{d}\mathbf{C}}{\mathrm{d}\mathbf{z}}\cdot\boldsymbol{\Gamma} - \dfrac{\partial \mathbf{L}}{\partial \mathbf{z}} & \mathbf{C} \end{bmatrix} \tag{13}$$

The terms from Eqs. 10–13 are inserted into Eq. 9; the implicit portion of the derivative becomes a triple product which is solved with the adjoint method. The adjoint vector does not contain the density of each element (**X**), and only needs to be solved once:

$$\mathbf{a} = \mathbf{A}^{-T} \cdot \frac{\partial g}{\partial \mathbf{r}} \tag{14}$$

The second derivative of the objective function is required if aerodynamic derivative metrics such as $C_{L\alpha}$ and $C_{m\alpha}$ are of interest. Two options are available for this computation. The first involves a similar analytical approach to the one described above. This would eventually necessitate the extremely difficult computation of $\partial\mathbf{A}/\partial\mathbf{r}$, which is seldom done in practice[25]. For the current work, only $\mathbf{C}$ depends on the aeroelastic state vector, while the rest of the Jacobian would be zero. Nonetheless, this remaining term $d^2\mathbf{C}/d\mathbf{z}^2$ is a four-dimensional tensor, and the computational complexities and cost associated with its construction is expected to be severe. As an alternative, finite differences are used here:

$$\frac{\partial g^2}{\partial \mathbf{X} \partial \alpha} \approx \frac{1}{\Delta\alpha} \cdot \left(\frac{\partial g}{\partial \mathbf{X}}(\alpha + \Delta\alpha) - \frac{\partial g}{\partial \mathbf{X}}(\alpha) \right) \tag{15}$$

The term $\partial g/\partial\alpha$ can be computed using another finite difference, or with the adjoint method described above, substituting the angle of attack for the element densities $\mathbf{X}$.

3.4. Optimization Procedure

In order to ensure the existence of the optimal wing topologies, a mesh-independent filter is employed. Such a filter acts as a moving average of the gradients throughout the membrane wing, and limits the minimum size of the imbedded carbon fiber structures[19]. As no constraints are included in the optimization, an unconstrained Fletcher-Reeves conjugate gradient algorithm[24] is employed. Step size is kept constant, at a reasonably small value to preserve the fidelity of the sensitivity analysis. In order to increase the chances of locating a global optimum, each optimization is run with three distinct initial designs: $X_o = 1$ (carbon fiber wing), $X_o = 0.5$, and $X_o = 0.1$. A pure membrane wing ($X_o = 0$) cannot be considered: inspection of the above equations reveals that when $X_o = 0$, the gradients become zero as well.

Six objective functions are considered: maximum lift, minimum drag, maximum L/D, maximum $C_{L\alpha}$, minimum $C_{L\alpha}$, and minimum $C_{m\alpha}$. Design and optimization with multiple performance criteria can be done my optimizing one variable with constraints upon the others (as discussed by Maute and Allen[15] for aeroelastic topology optimization). For MAV design however, the formulation and bounds of these constraints are uncertain, and the method does not provide a clear picture of the inherent trade-off between variables. The current work minimizes a convex combination of two objective functions for multi-objective optimization[9]. Successive optimizations with different relative weighting between the two metrics can fill out the Pareto optimal front. The computational cost of such an undertaking is large, and adequate location of the front is not ensured for non-convex problems. The objective function is now:

$$g = (1 - \delta) \cdot \left(\frac{f_1 - f_{1,\min}}{f_{1,\max} - f_{1,\min}} \right) + \delta \cdot \left(\frac{f_2 - f_{2,\min}}{f_{2,\max} - f_{2,\min}} \right) \tag{16}$$

where δ is a weighting parameter that varies between 0 and 1, and f_1 and f_2 are the two objective functions of interest. These functions are properly normalized, with the minimum and maximum bounds computed from the single-objective optimizations (optimizing with δ set as 0 or 1). This is cast as a minimization problem, and the sign of f_1 and f_2 is set accordingly. As before, the objective function can be augmented with the explicit penalty upon intermediate densities as needed.

4. SINGLE-OBJECTIVE OPTIMIZATION

The MAV wing under consideration has a Zimmerman planform, with a 152 mm wingspan, 124 mm root chord, and an aspect ratio of 1.25. 7° of positive geometric twist (nose up) is built into the wingtip, with 7° of dihedral between $2y/b = 0.4$ and the wingtip. Both a reflex airfoil and a singly-curved airfoil are studied (the former mitigates the pitching moment of the wing, and allows for the removal of a horizontal stabilizer to decrease the size of the MAV). Both have a maximum camber at the root of 6.8% (at $x/c = 0.22$), and the former airfoil has a maximum reflex at the root of –1.4% (at $x/c = 0.86$), as seen in Figure 4. Flight speed is kept constant at 13 m/s (equating to a Reynolds number of 10^5), but both 3° and 12° angles of attack are considered, with a $\Delta\alpha$ of 1° for finite differences. The flexural rigidity of the carbon fiber laminates is 0.5 N·m, and the pre-stress resultant of the latex membrane is 7 N/m. The thickness of the former is 0.5 mm, and the latter is 0.1 mm.

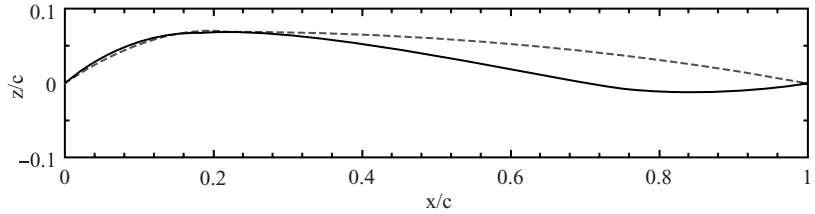

Figure 4. Singly-cambered and doubly-cambered (reflex) micro air vehicle airfoils.

The results in this section are meant to provide a general discussion as to the relationship between spatial stiffness distributions (i.e., wing topology) and aerodynamic load alleviation/augmentation for membrane MAV wings. Results pertaining to a compromise between these two design philosophies (multi-objective optimization) are given in the next section. Wing displacements and pressure distributions are given for select wing designs in Figure 5, for a reflex wing at 12° angle of attack. As the wing is modeled with no thickness in the vortex lattice method, distinct upper and lower pressure distributions are not available, only differential terms. Five topologies are discussed, beginning with a pure carbon fiber wing. Lift-augmentation designs are represented by a baseline PR wing and the topology optimized for maximum lift. Lift-alleviation designs are represented by a baseline BR wing and the topology optimized for minimum lift slope. As discussed, all optimal designs are computed with single-objective optimization.

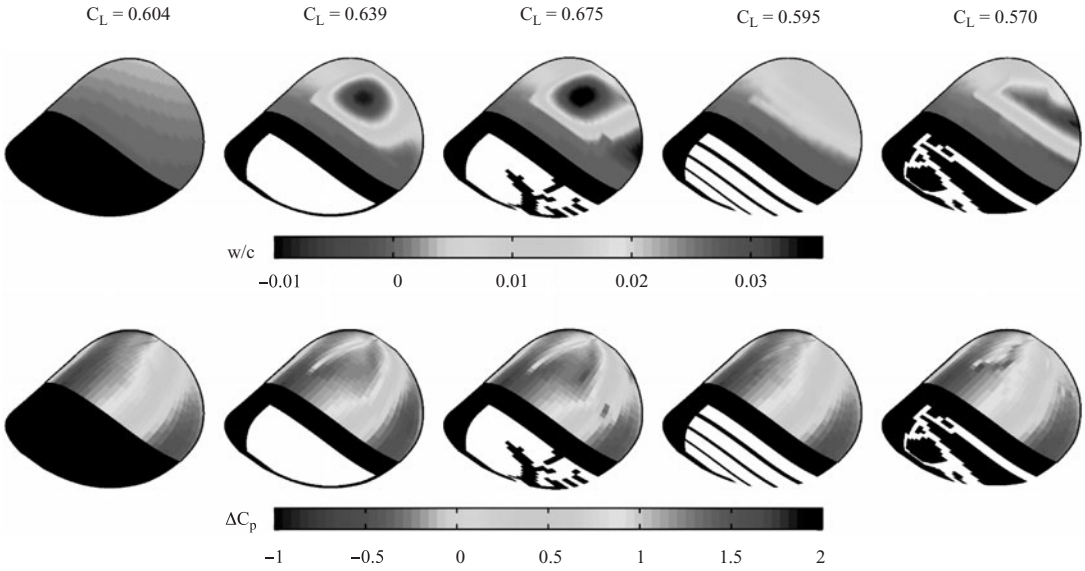

Figure 5. Normalized out-of-plane displacements (top) and differential pressure coefficients (bottom) for baseline and optimal topology designs, $\alpha = 12°$, reflex wing.

The differential pressure distribution over the monolithic carbon fiber wing is defined by leading edge suction due to flow stagnation, pressure recovery (and peak lift) over the maximum camber, and negative forces over the reflex portion of the wing. As expected, the inviscid solver misses the low-pressure cells at the wingtip (from the vortex swirling system), and the plateau in the pressure distribution, indicative of a separation bubble. This aerodynamic loading causes a moderate wash-in of the carbon fiber wing (0.1°), resulting in a computed lift coefficient of 0.604. Computed deformation of the PR wing is much larger than the carbon fiber wing, though the deformations are within the range of validity of a linear finite element solver. The sudden changes in wing geometry at the membrane/carbon fiber interfaces lead to sharp downward forces at the leading and trailing edges, the latter of which exacerbates the effect of the airfoil reflex. Despite this, the membrane inflation increases the camber of the wing and thus the lift, by 6.5% over the carbon fiber wing.

Several disparate deformation mechanisms contribute to the high lift of the MAV design located by the aeroelastic topology optimizer (middle column, Figure 5). First, the membrane inflation towards

the leading edge increases lift via cambering, similar to the PR wing (the pressure distributions over the two wing structures are identical through x/c = 0.25). The main trailing edge batten structure is then depressed downward along the trailing edge (due to the reflex) for wash-in, increasing the local angle of attack of each flexible wing section, and thus the lift. The local bending/twisting of this batten is minimal: the deformation along this structure is largely linear down the wing. The intersection of this linear trend with the curved inflated membrane shape produces a cusp in the airfoil. The small radius of curvature forces very large velocities, resulting in the lift spike at 46% of the chord. This combination of wash-in and cambering leads to a design which out-performs the lift of the PR wing by 5.6%.

Referring now to the load-alleviating MAV wing structures of Figure 5, the deformation of the BR wing is relatively small, allowing for just 0.1° of adaptive washout. The BR wing is very sensitive to pre-tensions in the span direction; the structure is too stiff. Furthermore, the reflex in the wing pushes the trailing edge down, limiting the ability of the battens to washout for load reduction. Less than a 2% drop in lift from the carbon fiber wing is obtained, and the pressure distributions of the two wings in Figure 5 are very similar. The load alleviating design located by the topology optimizer (right column, Figure 5) is significantly more successful. By filling the design space with patches of disconnected carbon fiber structures (dominated by a long batten which extends the length of the membrane skin, but is not connected to the wing's leading edge), the MAV wing is very flexible, but none of the membrane portions of the wing are large enough to camber the wing via inflation. Wing deformation is the same magnitude as that seen in the PR-type wings, but the motion is located at the trailing edge for adaptive washout, and lift is decreased by 5%. The local deformation within the membrane between the leading edge and the long batten structure is substantial, and the flow deceleration over this point sees a further loss in lift, as with the PR wing.

Similar results are given in Figure 6, for a cambered wing at 12° angle of attack. The three baseline wings are again shown (carbon fiber wing, PR, and BR), as well as the designs located by the single-objective topology optimization to maximize lift and minimize lift slope. As the forces are generally larger for the cambered airfoil, the deformations have increased to 5% of the root chord. The negative forces at the trailing edge of the airfoil are likewise absent. As before, the PR membrane wing effectively increases the lift over its carbon fiber counterpart through adaptive cambering, along with aerodynamic penalties from the shape discontinuities at the leading and trailing edge of the membrane skin.

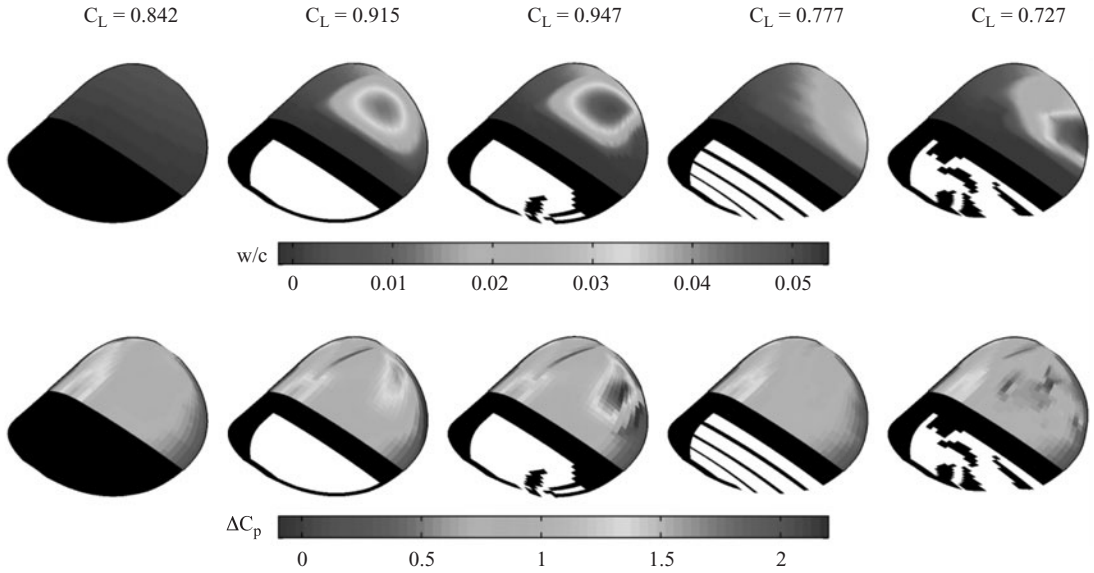

Figure 6. Normalized out-of-plane displacements (top) and differential pressure coefficients (bottom) for baseline and optimal topology designs, $\alpha = 12°$, cambered wing.

There is an appreciable amount of upward deformation of the PR wing's trailing edge carbon fiber strip, leading to washout of each flexible wing section, degrading the lift. As such, the aeroelastic topology optimizer can maximize lift (Figure 6, middle column) by adding more material to this strip

and negating the motion of the trailing edge. As discussed above, this strip does not continue unbroken to the wing tip, but ends at 65% of the semispan. The remaining trailing edge is filled with a free-floating batten. Such a configuration can (theoretically) improve the lift in several ways, similar to the trailing edge structure used for lift optimization in Figure 5.

Placing a flexible membrane skin between two rigid supports produces a trade-off: the cambering via inflation increases lift, but this metric is degraded by the sharp discontinuities in the airfoil shape. Towards the inner portion of the MAV wing, this trade-off is favorable for lift. Towards the wingtip however (either due to the changes in chord or in pressure) this is no longer true: the total lift can be increased by allowing this portion of the trailing edge to washout, thereby avoiding the negative pressures seen elsewhere along the trailing edge. The forward portion of this batten structure also produces a cusp in the wing geometry, forcing a very strong low pressure spike over the upper portion of the airfoil to increase the lift, as before. The inviscid solver probably over-predicts the strength of this spike: the presence of viscosity will attenuate the speed of the flow, and thus both the magnitude of the low pressure spike and its beneficial effect upon lift. The aeroelastic topology optimizer predicts a 3.5% increase in lift over the PR wing, and a 12.5% increase over the carbon fiber wing, though the veracity of these comparisons requires a viscous solver to ascertain the actual height of the low-pressure spike at x/c = 0.68.

The batten-reinforced design of Figure 6 is substantially more effective with the cambered wing, largely due to the positive forces at the trailing edge (rather than the negative forces seen over the reflex wing). The 1.6° of washout in the cambered BR wing decreases the load throughout most of the wing and decreases the lift by 8.5% (compared to the carbon fiber wing), but, as before, the load-alleviating design located by the topology optimizer (right column, Figure 6) is superior. Similar to above, the design utilizes a series of disconnected carbon fiber structures, oriented parallel to the flow, and extending to the trailing edge. The discontinuous wing surface forces a number of high-pressure spikes on the upper surface, notably at x/c = 0.2 and 0.6. This, in combination with the substantial adaptive washout at the trailing edge, decreases the lift by 13.6% over the carbon fiber wing and by 5.6% over the BR wing.

5. MULTI-OBJECTIVE OPTIMIZATION

Typical convergence history results are given in Figure 7, for simultaneous maximization of L/D and minimization of the lift slope. The weighting parameter δ is set to 0.5, for an equal convex combination of the two variables. The values given for $C_{L\alpha}$ (~ 0.4) are smaller than experimentally measured trends (~ 0.5, from Ref. 5), as the inviscid solver is unable to predict the vortex lift from the tip vortex swirling system[22]. Beginning with an intermediate density (X_o = 0.5), the optimizer is able to decrease the convex combination (g) from 0.7 to 0.3, using similar techniques seen above. All of the carbon fiber material adjacent to the root, leading edge, and wingtip is removed. Intersecting streams of membrane material grow across the wing, leaving behind disconnected carbon fiber structures. The lift-to-drag ratio converges after 25 iterations, while the lift slope requires 70 iterations to converge to a minimum value. An explicit penalty on intermediate densities is employed at 80 iterations, providing a moderate decrease in the combination objective function. The lift-to-drag ratio is improved as well through the penalty, though the lift slope suffers. The penalty only serves to force the density variables to 0 or 1, and does not significantly alter the wing topology.

The Pareto front for this same trade-off (maximum L/D and minimum $C_{L\alpha}$) is given in Figure 8, along with the performance of the 20 baseline MAV wing designs (Figure 1), and the design located by the single-objective topology optimizer to maximize $C_{L\alpha}$. All results are for a reflex wing at 3° angle of attack. Focusing first on the baseline wings, the BR and PR wings represent the extremes of the group in terms of lift slope, as expected. The homogenous carbon fiber wing has the lowest L/D (implying that for a reflex wing at this flight condition, any deformation will improve efficiency, regardless of the type), while a MAV design with 2 trailing edge battens has the largest L/D.

The aeroelastic topology optimization produces a set of designs that significantly out-perform the baselines, in terms of individually-considered metrics (maximum and minimum lift slope, maximum L/D), and multiple objectives: all of the baselines are removed from the computed Pareto front. The optimized designs lay consistency closer to the fictional utopia point as well , which for Figure 8 is at (4.18, 0.0366). The entirety of the Pareto front is not convex, but the topology optimizer is still able to adequately compute it. The data points are not evenly spaced either, with δ = 0.4 and 0.2 both very close to the solution with optimal L/D (δ = 0). This would suggest that despite the normalizing efforts,

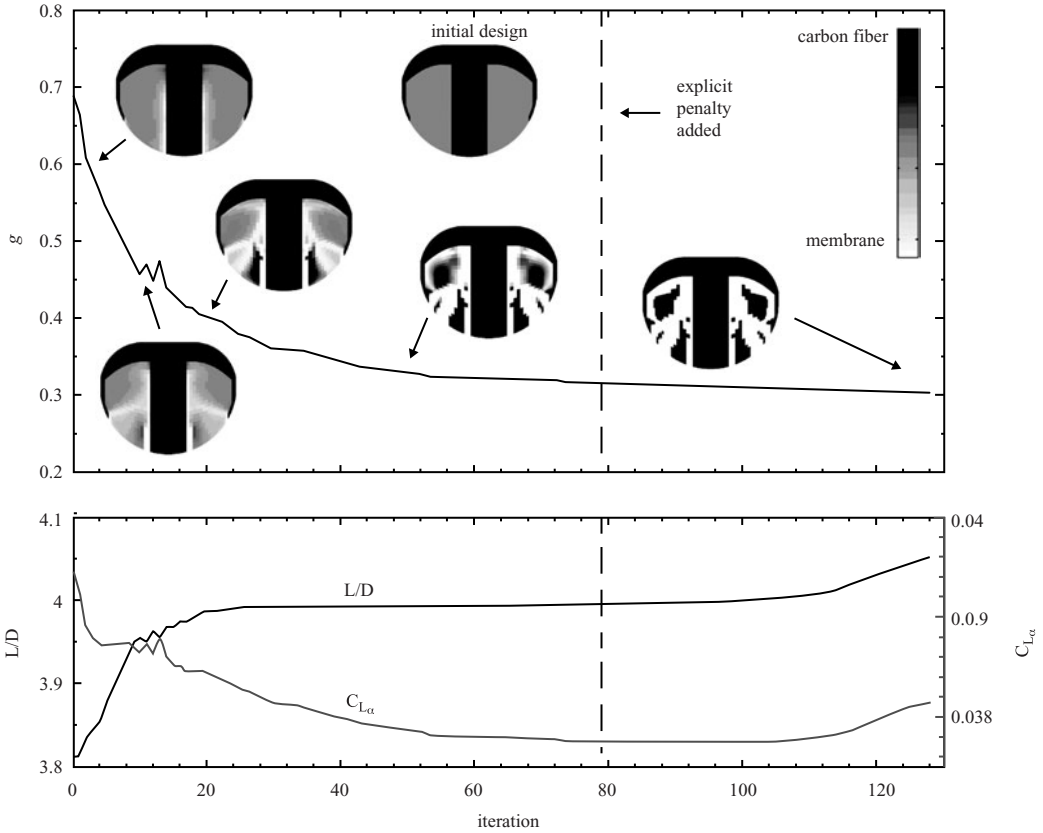

Figure 7. Convergence history for maximizing L/D and minimizing $C_{L\alpha}$, δ = 0.5, α = 3°, reflex wing.

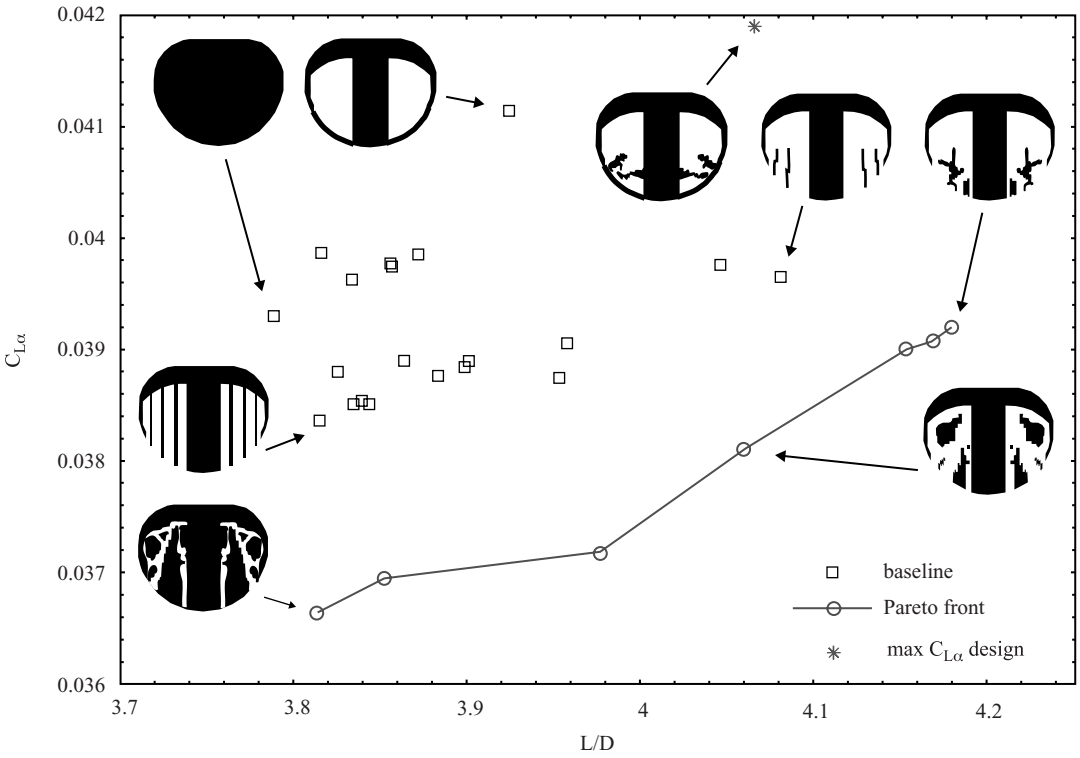

Figure 8. Trade-off between efficiency and lift slope, α = 3°, reflex wing.

maximizing L/D carries greater weight than minimizing the lift slope, an imbalance which may be remedied through nonlinear weighting[11].

In terms of the two metrics in Figure 8, none of the designs along the Pareto optimal front are technically superior: they are non-dominated, in that no other design exists within the data set that outperforms another design in both metrics. Other performance indices, not included in the optimization, can then be used to select an adequate design. For micro air vehicle applications, payload, flight duration, or agility/control metrics can be used, as discussed by Torres[26]. Realistic knowledge of the low-fidelity aeroelastic model's limitations or manufacturability concerns[27] may also be used to select a design. Wing displacements and pressure distributions for selected wings along the Pareto front of Figure 8 are given in Figure 9. Corresponding data along the spanwise section 2y/b = 0.58 is given in Figure 10. When $\delta = 1$ (single-objective optimization to minimize the lift slope), the aeroelastic topology optimizer locates a design very similar to that previously discussed in conjunction with Figure 5. Gradually adding weight to the L/D design metric removes the structures from the leading edge of the membrane skin, leaving batten-like structures at the trailing edge of the wing. The former transition allows the membrane to inflate and camber the wing, while the latter provides wash-in through depression of the trailing edge. The cambering membrane inflation does not grow monotonically with decreasing δ, but the trailing edge deformation does: from 0.25° of washout to 0.75° of wash-in. The size of the depressed trailing edge portion also grows in size. Decreasing δ shifts the lift penalty (pressure spike on the upper surface) forward towards the membrane/carbon fiber interface, and the lift spike (due to the surface geometry cusp at the leading edge of the batten structures) aft-ward. However, the design that maximizes L/D ($\delta = 0$) has no spike, with a smooth pressure and displacement profile aft of the lift penalty towards the leading edge. This may be indicative of the detrimental effect the airfoil cusp has on drag.

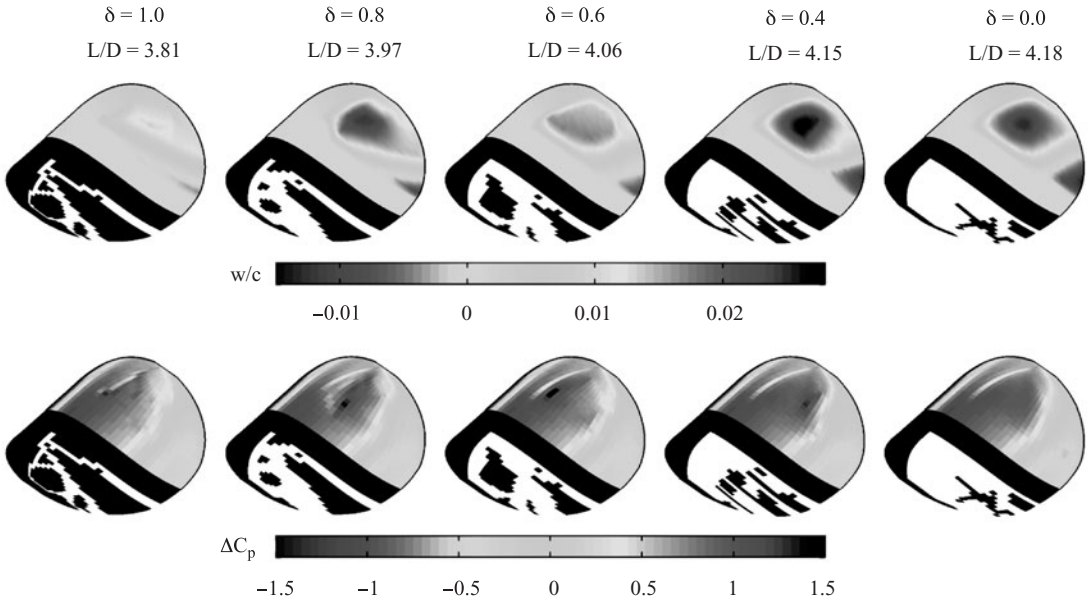

Figure 9. Normalized out-of-plane displacements (top) and differential pressure coefficients (bottom) for designs that trade-off between L/D and $C_{L\alpha}$, $\alpha = 3°$, reflex wing.

The trade-off between the drag and longitudinal static stability of a membrane MAV wing is very important: the latter is typically improved through large membrane inflations. The resulting tangent discontinuities in the wing surface produce pressure spikes oriented axially, and the exaggerated shape prompts the flow to separate above and below the membrane[5]. The trade-off is given in Figure 11 for a reflex wing at 12°, for both the 20 baseline designs and the Pareto front located with topology optimization. Compared with the data seen in Figure 8, the baseline designs at this higher angle of attack fail to adequately fill the design space; their performance generally falls within a band. The streamlining of the BR wing provides the lowest drag (of the baselines), but doesn't significantly outperform the homogenous carbon fiber wing.

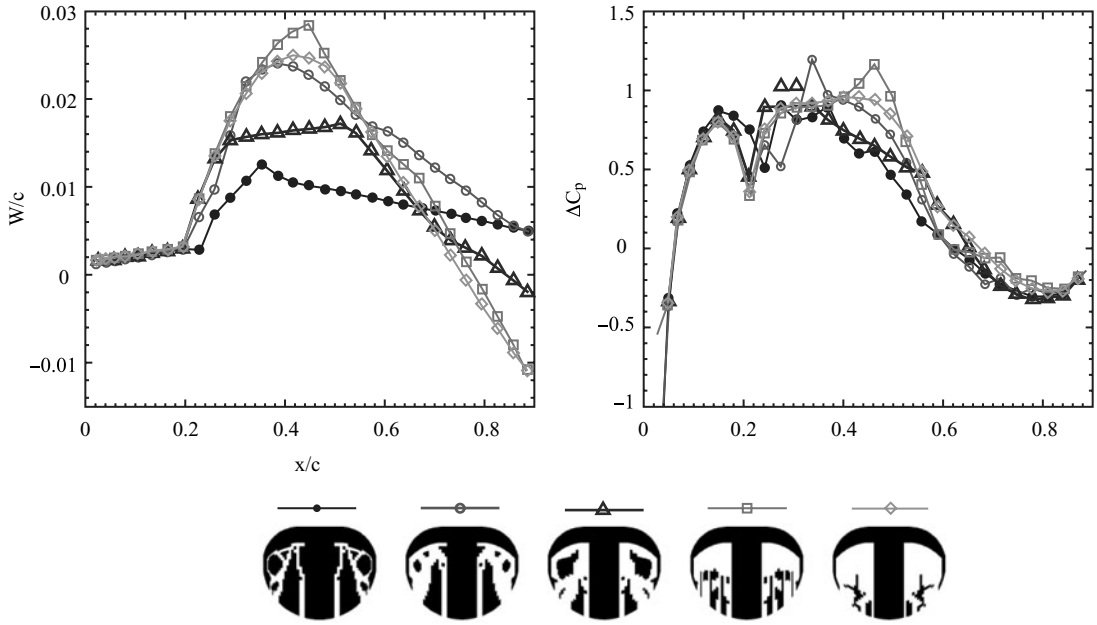

Figure 10. Deformations and pressures along 2y/b = 0.58 for designs that trade-off between L/D and $C_{L\alpha}$, $\alpha = 3°$, reflex wing.

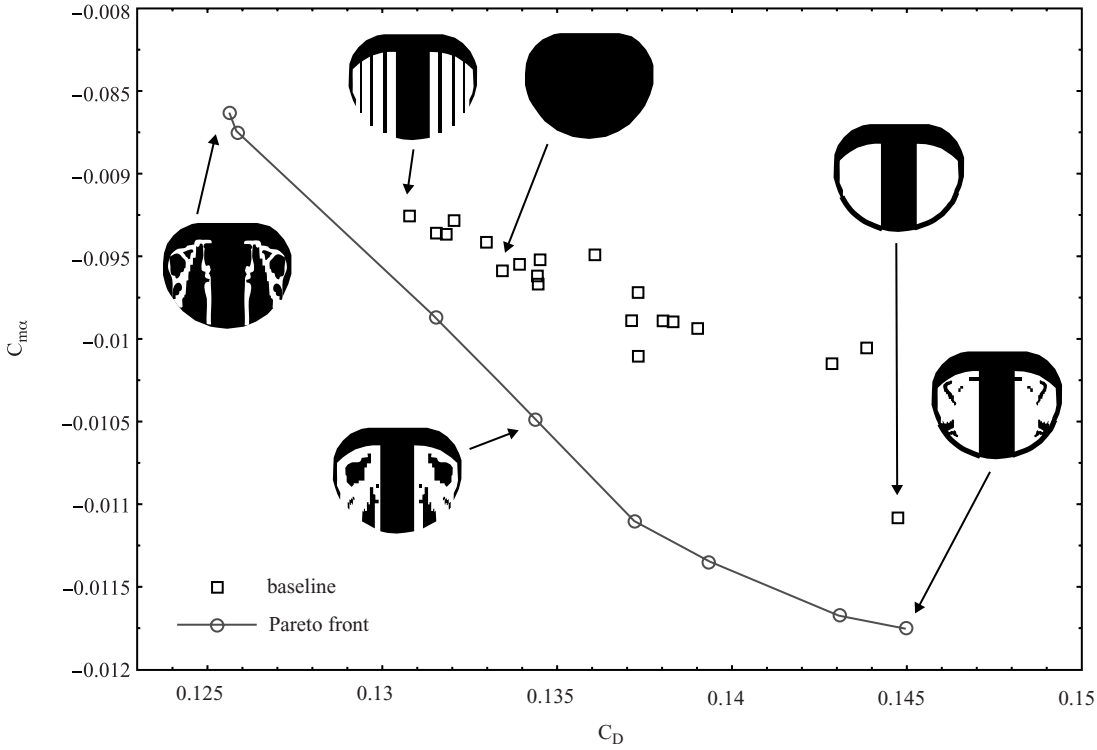

Figure 11. Trade-off between drag and pitching moment slope, $\alpha = 12°$, reflex wing.

As expected, the PR wing has the largest static stability margin of the baselines, but the drag penalty is large (and probably under-predicted by the inviscid flow solver). The topology optimizer is able to locate a design with the same drag penalty, but a steeper pitching moment slope: by 5.6% over the PR wing. The baseline designs, in general, lie closer to the Pareto front than seen in Figure 8, but the optimized designs are still superior in terms of Pareto optimality and individual metrics. The optimal drag design (3.8% less than the BR wing) begins with two carbon fiber structures imbedded within the

membrane skin, one of which is a long batten that extends the length of the design domain. By adding weight to the static stability metric ($C_{m\alpha}$), this long batten breaks in two pieces; the foreword section shrinks into a slender batten imbedded in the leading edge of the membrane skin. The aft-ward section gradually accumulates along the trailing edge, merges with the root, and forms the trailing edge support. As discussed above, this reinforcement does not connect monolithically to the wingtip; this space is filled with a trailing edge batten. The Pareto optimal front of Figure 11 shows a more pronounced convexity than seen in Figure 8, though the data points are still not evenly spaced with δ.

Similar data is given in Figure 12, for the trade-off between maximum lift and minimum lift slope, for a cambered wing (no reflex) at 12° angle of attack. Such a trade-off is of interest because minimizing the lift slope of a membrane MAV wing, while an effective method for delaying the onset of stall or rejecting a sudden wind gust, typically decreases the pre-stall lift in steady flight as well; a potentially unacceptable consequence. Certain aeroelastic deformations, such as a passive wing de-cambering, would provide a wing with higher lift (than the baseline carbon fiber wing, for example), but a shallower lift slope. Such a motion is unusual for low aspect ratio membrane structures however: none of the baseline designs in Figure 12 have both larger lift and a smaller lift slope than the carbon fiber wing. The correlation between C_L and $C_{L\alpha}$ within the set of baseline designs is very strong, and all the designs fall very close to a single line, clustered in three groups. Any baseline design with adaptive washout (free trailing edge) has lift slopes between 0.035 and 0.037, any overly-stiff design with battens oriented perpendicular to the flow (or the carbon fiber wing) has a slope between 0.038 and 0.039, and the PR wing has a lift slope of 0.041.

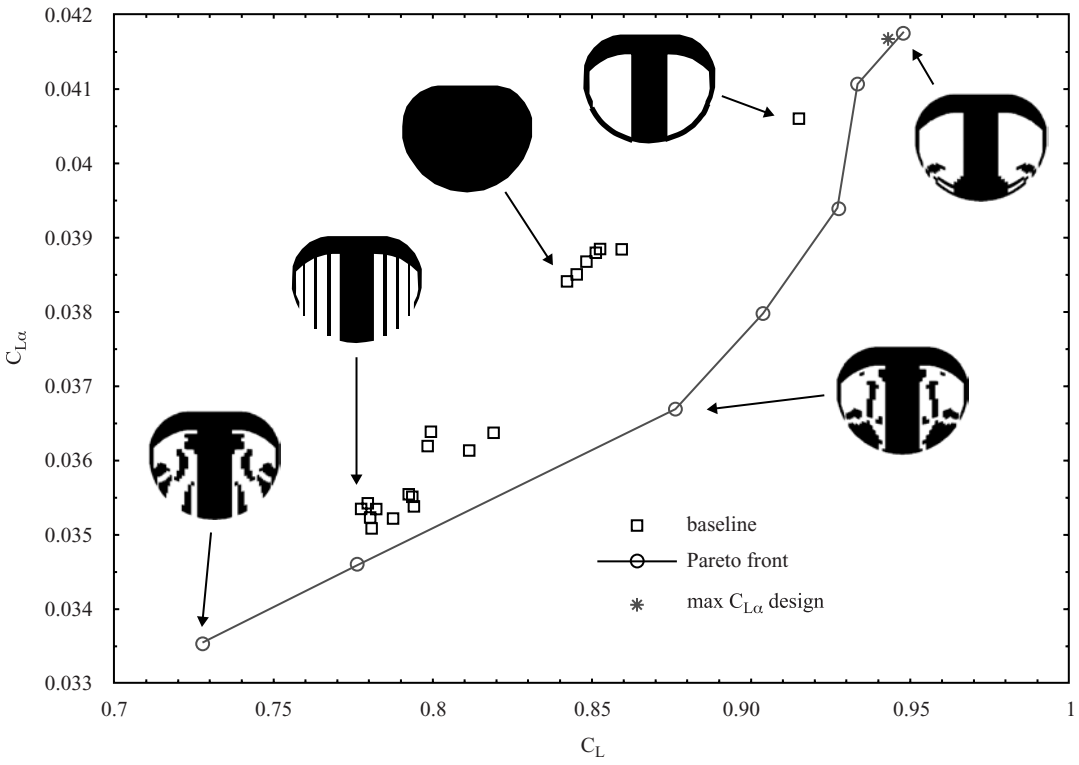

Figure 12. Trade-off between lift and lift slope, $\alpha = 12°$, cambered wing.

The strong data correlation is in sharp contrast to the results of Figure 8 for the reflex wing, where the baseline structures are well-distributed through the design space. This emphasizes the large role that the doubly-curved airfoil can play in producing many different types of aeroelastic deformation, providing greater freedom to the designer and better compromise designs. Despite this, the magnitude of the variability is higher for the cambered wing, as the forces are generally larger: $C_{L\alpha}$ can be varied by 14.5% for the reflex wing in Figure 8, but by 26.4% for the cambered wing in Figure 12. These numbers can be increased further with the use of nonlinear membrane structures, but deformations must be kept at a moderate level to preserve the fidelity of the linear finite element model in the current work.

As wing structures with high lift and shallow lift slopes are rare, the set of baseline designs lies close to the Pareto front in Figure 12. None are superior however, in terms of individual metrics or Pareto optimality. The designs located by the topology optimizer to maximize lift and maximize lift slope are almost identical. The PR wing is effective for cambered wings at higher angles of attack, and lies close to these two optimums. The slight convexity in the Pareto front produces two designs with the sought-after higher lift and lower lift slope than the solid carbon fiber wing. The topology given in Figure 12 increases the lift coefficient from 0.842 to 0.876 and decreases the lift slope from 0.038 to 0.036, and is found from equal weighting of the two metrics ($\delta = 0.5$).

Wing displacements and pressure distributions for selected wings along the Pareto front of Figure 12 are given in Figure 13. Corresponding data along the spanwise section 2y/b = 0.58 is given in Figure 14. Shallow lift slopes are provided with a series of disconnected batten structures oriented parallel to the flow. As a weight for high lift is added to the objective function, a large carbon fiber region grows at the trailing edge, but is connected to neither the root or the wing tip. This allows for both washout and membrane cambering, and produces the MAV design with higher lift and shallower lift slopes than the carbon fiber wing ($\delta = 0.5$). Further decrease in δ flattens the chord of the trailing edge structure and removes the disjointed battens at the leading edge, to maximize lift.

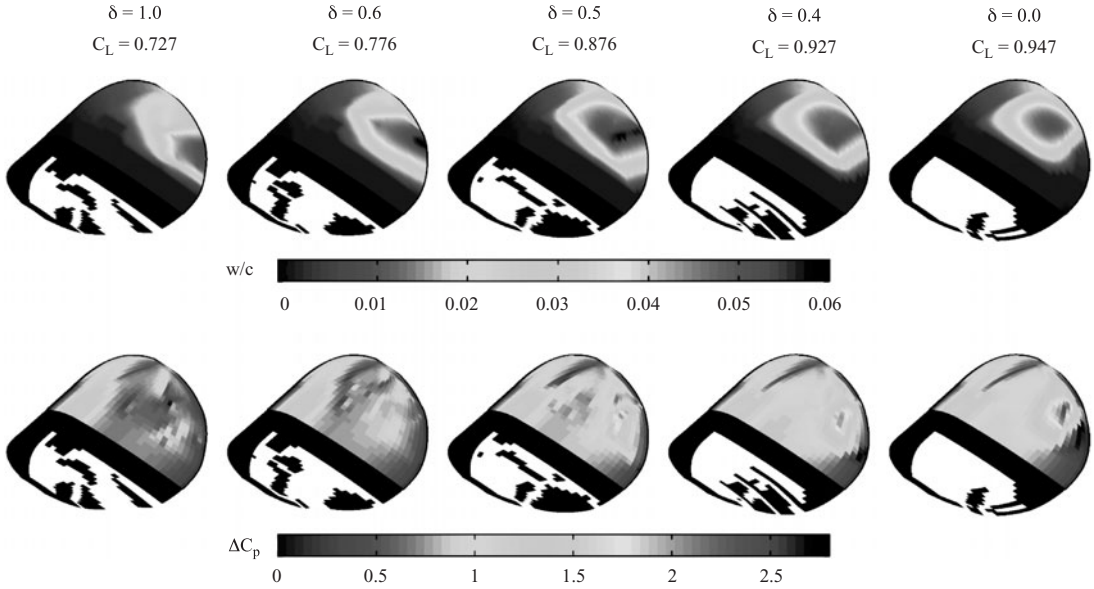

Figure 13. Normalized out-of-plane displacements (top) and differential pressure coefficients (bottom) for designs that trade-off between C_L and $C_{L\alpha}$, $\alpha = 12°$, cambered wing.

The locus of aeroelastic deformation clearly shifts from the trailing edge to the mid-chord of the wing as the structures produce higher lift. Washout monotonically decreases with δ (from 3° to 0.1° of wash-in). Membrane deformations are largest when $\delta = 0.5$, though the design that maximizes lift shows the largest change in camber, owing to the significant adaptive washout of the former, as discussed. Similarly, the aerodynamic penalty at the leading edge of the membrane/carbon fiber interface is largest with the compromise design. The severity of the surface cusp (and the concomitant lift spike) increases with decreasing δ, emphasizing its usefulness as a lift-augmentation device. As discussed above, the severity of this spike is certainly over-predicted by the inviscid flow solver, though similar trends are seen using Navier-Stokes solvers for wings with tangent discontinuities[5].

6. EXPERIMENTAL VALIDATION

Due to the low-fidelity nature of the aeroelastic analysis employed in this work, a certain measure of experimental validation of the superiority of computed optima over baseline designs is required. This is particularly true for drag-based metrics, which, as discussed above, the vortex lattice method will struggle to accurately compute. For this purpose, 6 designs are built for experimental testing: three baseline designs (monolithic carbon fiber wing, PR, and BR wings), and three topologically-optimized

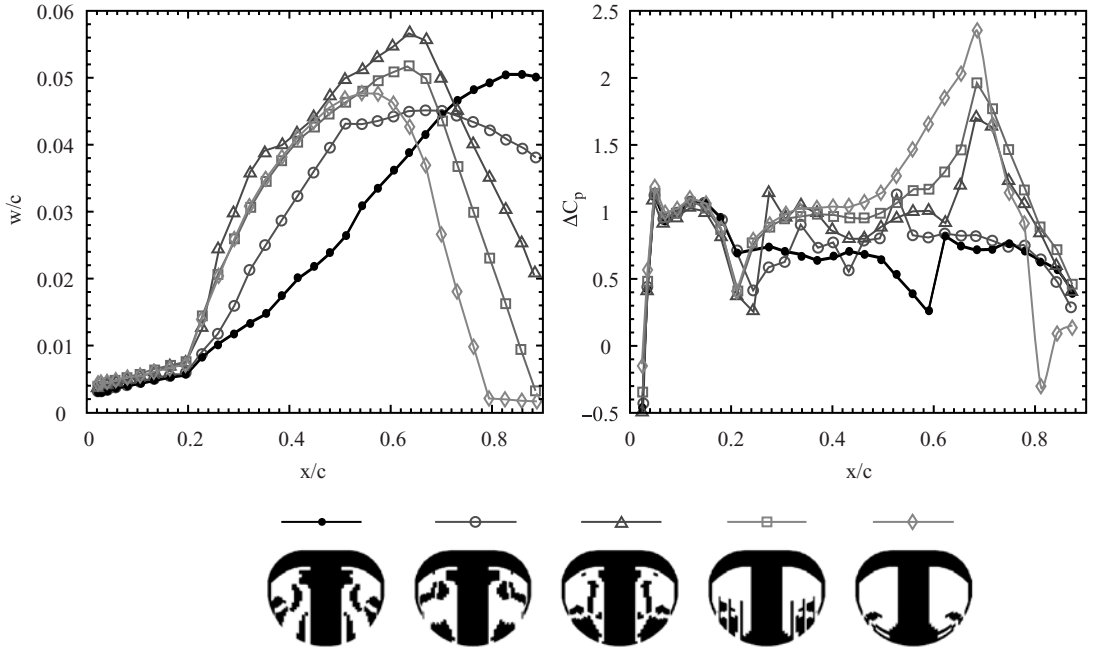

Figure 14. Deformations and pressures along $2y/b = 0.58$ for designs that trade-off between C_L and $C_{L\alpha}$, $\alpha = 12°$, cambered wing.

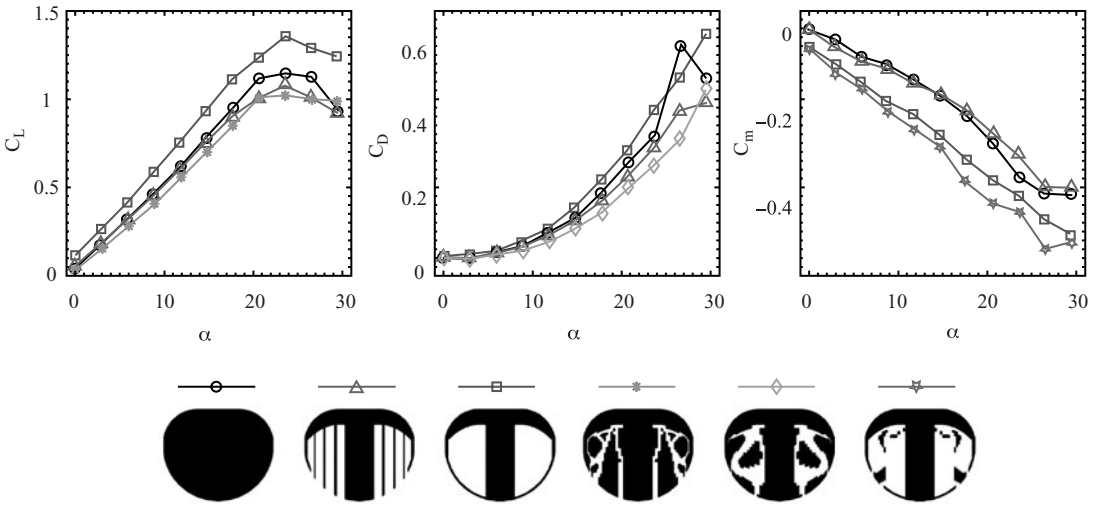

Figure 15. Experimentally measured forces and moments for baseline and optimal topology designs, reflex wing.

designs (minimum $C_{L\alpha}$, minimum drag, and minimum $C_{m\alpha}$, the fourth, fifth, and sixth wings shown in Figure 15). The latter three designs are found by single-objective optimization with a reflex airfoil, at 3° angle of attack. Multi-objective optimization and Pareto optimality are not considered in this section. All testing is conducted in a closed-loop wind tunnel, and loads are measured with a strain gage sting balance through an entire α-sweep; more details pertaining to the experimental testing can be found by Stanford et al.[5]

Experimental results are given in Figure 15, in terms of C_L, C_D, and C_m of the three baseline designs and the relevant optimal design. All three structures located by the topology optimizer show marked improvements over the baseline experimental data, validating the use of a low fidelity aeroelastic model as a surrogate for computationally-intensive nonlinear models. With the exception of very low (where

deformations are small) and very high angles of attack (where the wing has stalled), the optimized designs consistently out-perform the baselines. The minimum $C_{L\alpha}$ design has a shallower lift slope than the BR wing, and a flatter stalling curve (left of Figure 15). The minimum drag design similarly out-performs the BR wing (middle of Figure 15). The minimum $C_{m\alpha}$ design has a steeper pitching moment slope than the PR wing (right of Figure 15), indicative of a longer static stability margin.

7. CONCLUSIONS

Aeroelastic topology optimization has been used to design the laminate reinforcement of a membrane micro air vehicle wing, with a two-material formulation on the wetted surface. The static aeroelasticity is modeled with a vortex lattice method coupled to linear membrane and shell elements. The sensitivity of the wing's aerodynamic performance to each element density is computed with an adjoint analytical sensitivity analysis. Pareto trade-off curves are constructed by taking a convex combination of two conflicting objective functions, with varied weights between the two. The following conclusions can be drawn:

1. The optimizer makes use of several disparate phenomena for lift augmentation: membrane inflation to camber the wing, depression of the trailing edge for wash-in, and sharp cusps in surface geometry that cause the pressure to locally spike.
2. Optimal load-alleviation is obtained with a series of disjointed laminate structures: the wing is flexible enough to substantially washout at the trailing edge, but the remaining membrane patches aren't large enough to locally inflate, which would add camber and increase the lift.
3. For all cases, the topology optimizer is able to locate a series of designs that outperform the baselines in terms of both individual and compromise flight metrics.
4. Reflex airfoils play an important role in providing a large variety of potential aeroelastic responses, while singly-cambered airfoils provide a larger range (higher forces).
5. The topology optimizer can compute designs with an adequate compromise between load alleviation and augmentation, through a unique combination of cambering via inflation and trailing edge washout.
6. Relevant improvements in aerodynamic performance can be obtained despite the low-fidelity aeroelastic model employed, as indicated by experimental testing.

This work has clearly demonstrated the feasibility of aeroelastic topology optimization for membrane wings; future work will concentrate on two areas. First, the overall aeroelastic model fidelity will be increased to encompass nonlinear membrane mechanics and viscous flow solvers. Despite the obvious improvements over the baseline designs found in this work (and confirmed in the wind tunnel), including the massive nonlinearities known to characterize MAV flight may provide true optima. The two models (low and high fidelity) need not be used separately, in order to ease the burden in terms of computational cost. Second, the topology optimization will be extended to unsteady flows, keeping the overall level of model fidelity at a similar level to that found in this work. As discussed above, the vortex lattice method can be extended to unsteady flows by discretizing the wake. Such an algorithm can then be use to optimize wing structures within unsteady gusts, or during flapping flight.

ACKNOWLEDGMENTS

This work was jointly supported by the Air Force Research Laboratory and the Air Force Office of Scientific Research under the MURI program F49620-03-1-0381.

REFERENCES

1. Combes, S., Daniel, T., "Flexural Stiffness in Insect Wings I. Scaling and the Influence of Wing Venation," *Journal of Experimental Biology*, Vol. 206, No. 17, pp. 2979–2987, 2003.
2. Shyy, W., Lian, Y., Tang, J., Liu, H., Trizila, P., Stanford, B., Bernal, L., Cesnik, C., Friedmann, P., Ifju, P., "Computational Aerodynamics of Low Reynolds Number Plunging, Pitching, and Flexible Wings for MAV Applications," *Acta Mechanica Sinica*, Vol. 24, No. 4, pp. 351–373, 2008.
3. Song, A., Tian, X., Israeli, E., Galvao, R., Bishop, K., Swartz, S., Breuer, K., "Aeromechanics of Membrane Wings with Implications for Animal Flight," *AIAA Journal*, Vol. 46, No. 8, pp. 2096–2106, 2008.
4. Wilkinson, M., "Sailing the Skies: The Improbable Aeronautical Success of the Pterosaurs," *Journal of Experimental Biology*, Vol. 210, No. 5, pp. 1663–1671, 2007.

5. Stanford, B., Ifju, P., Albertani, R., Shyy, W., "Fixed Membrane Wings for Micro Air Vehicles: Experimental Characterization, Numerical Modeling, and Tailoring," *Progress in Aerospace Sciences*, Vol. 44, No. 4, pp. 258–294, 2008.
6. Eschenauer, H., Olhoff, N., "Topology Optimization of Continuum Structures: A Review," *Applied Mechanics Review*, Vol. 54, No. 4, pp. 331–390, 2001.
7. Bendsøe, M., Lund, E., Olhoff, N., Sigmund, O., "Topology Optimization: Broadening the Areas of Application," *Control and Cybernetics*, Vol. 34, No. 1, pp. 7–35, 2005.
8. Patel, N., Tillotson, D., Renaud, J., Tovar, A., Izui, K., "Comparative Study of Topology Optimization Techniques," *AIAA Journal*, Vol. 46, No. 8, pp. 1963–1975, 2008.
9. Chen, T., Wu, S., "Multiobjective Optimal Topology Design of Structures," *Computational Mechanics*, Vol. 21, No. 6, pp. 483–492, 1998.
10. Nishiwaki, S., Frecker, M., Min, S., Kikuchi, N., "Topology Optimization of Compliant Mechanisms using the Homogenization Method," *International Journal for Numerical Methods in Engineering*, Vol. 42, No.3, pp. 535–559, 1998.
11. Min, S., Nishiwaki, S., Kikuchi, N., "Unified Topology Design of Static and Vibrating Structures Using Multiobjective Optimization," *Computers and Structures*, Vol. 75, No. 1, pp. 93–116, 2000.
12. Balabanov, V., Haftka, R., "Topology Optimization of Transport Wing Internal Structure," *Journal of Aircraft*, Vol. 33, No. 1, pp. 232–233, 1996.
13. Krog, L., Tucker, A., Kemp, M., "Topology Optimization of Aircraft Wing Box Ribs," *AIAA/ISSMO Multidisciplinary Analysis and Optimization Conference*, Albany, NY, August 30–September 1, 2004.
14. Luo, Z., Yang, J., Chen, L., "A New Procedure for Aerodynamic Missile Designs Using Topological Optimization Approach of Continuum Structures," *Aerospace Science and Technology*, Vol. 10, No. 5, pp. 364–373, 2006.
15. Maute, K., Allen, M., "Conceptual Design of Aeroelastic Structures by Topology Optimization," *Structural and Multidisciplinary Optimization*, Vol. 27, No. 1, pp. 27–42, 2004.
16. Maute, K., Reich, G., "Integrated Multidisciplinary Topology Optimization Approach to Adaptive Wing Design," *Journal of Aircraft*, Vol. 43, No. 1, pp. 253–263, 2006.
17. Gomes, A., Suleman, A., "Topology Optimization of a Reinforced Wing Box for Enhanced Roll Maneuvers," *AIAA Journal*, Vol. 46, No. 3, pp. 548–556, 2008.
18. Ifju, P., Jenkins, D., Ettinger, S., Lian, Y., Shyy, W., Waszak, M., "Flexible-Wing-Based Micro Air Vehicles," *Confederation of European Aerospace Societies Aerodynamics Conference*, London, UK, June 10–12, 2003.
19. Bendsøe, M., Sigmund, O., *Topology Optimization*, Springer-Verlag, Berlin, Germany, 2003.
20. Stanford, B., Ifju, P., "Aeroelastic Topology Optimization of Membrane Structures for Micro Air Vehicles," *Structural and Multidisciplinary Optimization*, DOI 10.1007/s00158-008-0297-x, 2008.
21. Cook, R., Malkus, D., Plesha, M., Witt, R., *Concepts and Applications of Finite Element Analysis*, Wiley, New York, NY, 2002.
22. Katz, J., Plotkin, A., *Low-Speed Aerodynamics*, Cambridge University Press, Cambridge, UK, 2001.
23. Stanford, B., Abdulrahim, M., Lind, R., Ifju, P., "Investigation of Membrane Actuation for Roll Control of a Micro Air Vehicle," *Journal of Aircraft*, Vol. 44, No. 3, pp. 741–749, 2007.
24. Haftka, R., Gürdal, Z, *Elements of Structural Optimization*, Kluwer, Dordrecht, The Netherlands, 1992.
25. Maute, K., Nikbay, M., Farhat, C., "Sensitivity Analysis and Design Optimization of Three-Dimensional Non-Linear Aeroelastic Systems by the Adjoint Method," *International Journal for Numerical Methods in Engineering*, Vol. 56, No. 6, pp. 911–933, 2002.
26. Torres, G., "Aerodynamics of Low Aspect Ratio Wings at Low Reynolds Numbers with Applications to Micro Air Vehicle Design," Ph.D. Dissertation, Department of Aerospace and Mechanical Engineering, University of Notre Dame, South Bend, IN, 2002.
27. Lyu, N., Saitou, K., "Topology Optimization of Multicomponent Beam Structure via Decomposition-Based Assembly Synthesis," *Journal of Mechanical Design*, Vol. 127, No. 2, pp. 170–183, 2005.